pcim
EUROPE

Optimized Modulation of Isolated Bidirectional Single-Stage Three-/Single-Phase X-Rectifier for EV On-Board Chargers

Sven Weihe, Johann W. Kolar, Jonas Huber

Advanced Mechatronic Systems Group, ETH Zürich, Switzerland

Corresponding author: Sven Weihe, weihe@lem.ee.ethz.ch
Speaker: Sven Weihe, weihe@lem.ee.ethz.ch

Abstract

The three-/single-phase ac input single-stage isolated eXtended-functionality rectifier (X-Rectifier) EV on-board charger (OBC) employs 650 V GaN monolithic bidirectional power transistors (M-BDS) in the input stage, provides sinusoidal input currents and bidirectional operation in three-phase and split/single-phase grids without power derating, operates from asymmetrical three-phase mains, provides reactive power if needed, and supports extremely asymmetric phase loading in islanding/standalone mode. This paper first presents an improved X-Rectifier standard modulation method (M#1) with significantly lower current stresses compared to a previously published proof-of-concept method while being applicable for all operating modes discussed above. Next, the optimization of M#1 regarding semiconductor losses is discussed and the implementation of near-optimum secondary-side duty-cycle calculation (named M#2) without requiring high-dimensional look-up-tables is introduced. Considering a 6.6 kW X-Rectifier and a typical charging process, simulation results indicate an improvement of the average semiconductor efficiency from 98.6% for M#1 to 98.9% for M#2, i.e., a semiconductor loss reduction of about 20%.

1 Introduction

Next-generation electric vehicle (EV) on-board chargers (OBCs) must provide sinusoidal input currents, galvanic isolation, high power density, bidirectional power exchange with a three-phase or a split/single-phase mains without derating, a wide battery dc voltage range (e.g., 250 V to 450 V), and, in particular, extended functionality such as vehicle-to-grid (V2G) or vehicle-to-load (V2L) modes (e.g., acting as a standalone power source on a construction site) [1], where potentially very strong imbalances in the loading of the phases must be expected. Aiming for improving the power density and lowering the realization effort of today's prevailing two-stage topologies (ac-dc rectifier and isolated dc-dc converter), various single-stage topologies have been investigated over the past two decades [2]–[13] with some featuring compatibility with three-phase *and* single-phase grids [5], [14], [15].

The recently proposed eXtended-functionality rectifier (X-Rectifier) [16] shown in **Fig. 1** is a promising single-stage topology which provides all features of next-generation OBCs listed above and, due to the

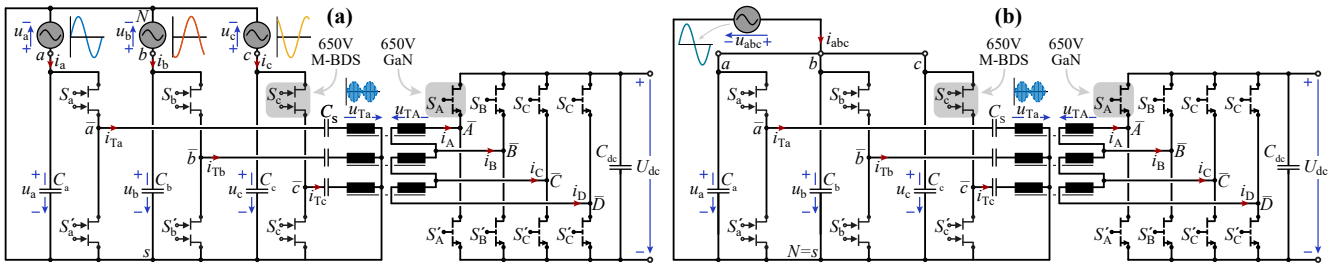

Fig. 1: Extended-functionality rectifier (X-Rectifier) utilizing 650 V GaN monolithic bidirectional power transistors in the ac front-end to directly interface with either **(a)** a three-phase (400 V line-to-line rms, 325 V_{peak} line-to-neutral) or **(b)** a single-phase (325 V_{peak} line-to-neutral) grid. Note the connection between the HF transformer star point and the primary-side switching stage neutral s [16].

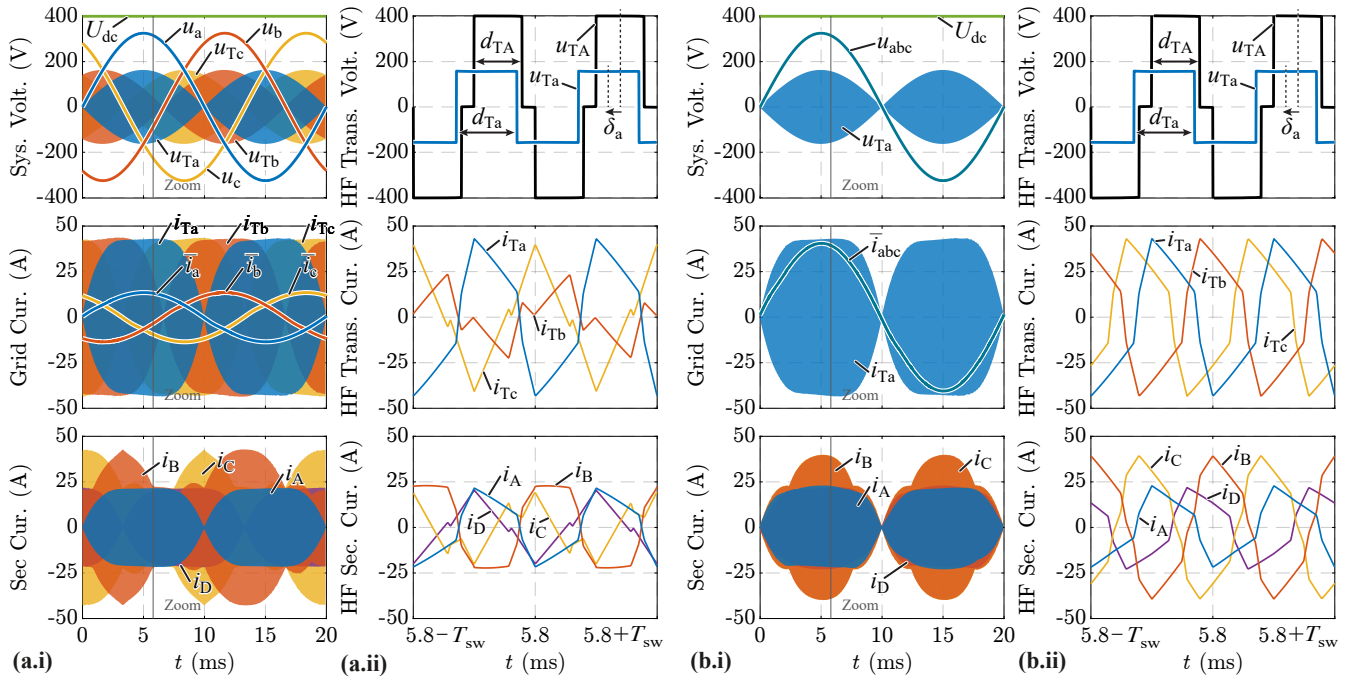

Fig. 2: Simulated key waveforms of the X-Rectifier from **Fig. 1** (specifications and component values from **Tab. 1**) using the proposed standard secondary-side modulation M#1 and the control scheme from **Fig. 4** for **(a)** three-phase and **(b)** single-phase PFC operation over **(i)** a mains period (U_{dc} = 400 V, P = 6.6 kW) and **(ii)** two switching periods T_{sw} around t = 5.8 ms. Note that the transformer/bridge-leg currents are significantly lower than those obtained with the proof-of-concept modulation used in [16].

phase-modular input, i.e., star-connection of the input stage bridge-legs, can be realized with 650 V GaN monolithic bidirectional switches (M-BDSs) [17], [18] when interfacing a 400 V (line-to-line rms) three-phase grid and is capable of delivering the same rated power in three-phase and single-phase configuration.

The X-Rectifier features a connection from the primary-side high-frequency (HF) transformer star point to the switching stage neutral s, which decouples the phases on the primary side, and the open-delta connection of the secondary-side transformer windings to a four-leg switching stage allows three secondary-side transformer winding voltages with independent duty cycles. Thus, fully decoupled power flow regulation in all three mains phases is possible, whereas fewer components than in fully phase-modular topologies (e.g., with a full-bridge circuit on the primary and secondary side of each phase) are used. However, the proof-of-concept modulation method employed in [16] results in relatively high current stresses, increased secondary-side switching frequency, and unfavourable design constraints.

Therefore, this paper presents an improved modulation method (M#1) that removes these drawbacks in **Section 2**, explaining the operating principle and grid current control for three-phase and single-phase operation. Then, **Section 3** highlights the X-Rectifier's extended functionality, i.e., the capability to deal with abnormal operating conditions such as an asymmetric grid and to provide reactive power support as well as an islanding mode for V2L scenarios. Finally, **Section 4** investigates the optimization of M#1 using a numerical model of the X-Rectifier, and proposes a near optimal modulation scheme M#2 reducing the mission-profile semiconductor losses by 21%. **Section 5** concludes the paper.

2 Operating Principle

To explain the operating principle, **Fig. 2** shows simulated key waveforms of the X-Rectifier from **Fig. 1**. In both, three-phase and single-phase grid connections (see **Fig. 1**), the ac-front-end semiconductors are switched with a fixed duty cycle of 50%, translating the grid input voltages u_{a}, u_{b}, u_{c} into mains frequency amplitude modulated HF voltages. These are applied to the series capacitors C_{S} and the primary-side transformer windings, whereby the aforementioned star point connection of the X-Rectifier (from HF transformer star point

Tab. 1: Considered system specifications and key component realizations.

Parameter	Symbol	Value	Unit
Grid Voltage[1]	3ϕ, $u_{\mathrm{a,b,c}}$	230	V_{rms}
	1ϕ, u_{abc}	230	V_{rms}
Grid Freq.	f_{ac}	50	Hz
Switching Freq.	f_{sw}	72	kHz
Output Voltage	U_{dc}	250...450	V
Rated Power	P	±6.6	kW
Input Cap.	C_{a}	2.5	µF
M-BDS	S_{a},S'_{a}	25	$m\Omega_{typ}$
		650	V
Series Cap.	C_{S}	10	µF
Leakage Ind.	L_{S}	8	µH
Turns Ratio	$N_1 : N_2$	1:2	
DC Side Semi.	S_{A},S'_{A}	25	$m\Omega_{typ}$
		650	V

[1] line-to-neutral

to switching stage neutral s) ensures phase decoupling of the applied voltages. The series capacitors C_{S} block the low-frequency (LF) voltage components, e.g., the 50 Hz component, and thus only the HF components varying between $\pm\frac{1}{2}u_{\mathrm{a}}$, $\pm\frac{1}{2}u_{\mathrm{b}}$, $\pm\frac{1}{2}u_{\mathrm{c}}$ act on the primary windings of the transformers (see u_{Ta}, u_{Tb}, u_{Tc} in **Fig. 2a.i**).[1]

Employing secondary-side transformer voltage waveforms with equal voltage time areas per pulse as those on the primary side [9], [10] results in (roughly) equal reactive power processed by the primary-side and the secondary-side bridges and hence in (roughly) minimal conduction losses [19], [20] (yet not necessarily in overall minimum semiconductor losses, see **Section 4**). With the primary-side transformer HF voltage of phase j being a square wave with time-varying amplitude $u_{\mathrm{j}}/2$ with $j \in \{a, b, c\}$, the secondary-side duty cycles are therefore

$$d_{\mathrm{TJ}} = \frac{u_{\mathrm{j}}}{2U_{\mathrm{dc}}}\frac{N_2}{N_1} \tag{1}$$

with $J \in \{A, B, C\}$, U_{dc} denoting the output voltage and N_1/N_2 the transformer turns ratio.

[1] Here, three separate transformers are considered, but preliminary investigations indicate that magnetic integration / a four-limb transformer could be employed.

The phase shift δ_{j} between the HF primary-side and secondary-side transformer voltages (see **Fig. 2**) adjusts the power flow as in any dual active bridge (DAB) converter; it is roughly constant over the mains period in steady state [13], [16], [21].

Advantageously, even without closed-loop grid current control, approximate power-factor correction (PFC) behaviour, i.e., mains voltage proportional (sinusoidal) current consumption is achieved [21]: Considering a first-harmonic approximation, the power transfer in a DAB converter is proportional to the voltage amplitudes applied on either side of the transformer. Here, the power transfer in phase j is thus $P_{\mathrm{j}} \propto u_{\mathrm{j}} \cdot d_{\mathrm{TJ}}U_{\mathrm{dc}} \propto u_{\mathrm{j}}^2$, i.e., proportional to the instantaneous mains voltage u_{j} squared, which corresponds to a resistive load.

The proof-of-concept modulation method for the X-Rectifier previously used in [16] focuses on maintaining a *synchronous* switching operation of the ac front-end bridge-legs as, e.g., in [9]. However, this comes at the cost of having the secondary side operate at an increased switching frequency along with requiring an unfavourable transformer turns ratio N_1/N_2 to facilitate single-phase operation, which results in especially high secondary-side current stress on the transformer and bridge-legs.

2.1 Secondary-Side Modulation

To more efficiently operate the X-Rectifier, secondary-side transformer voltages u_{TJ} with arbitrary effective duty cycles d_{TJ} can be generated with the four-leg switching stage employing the modulation approach proposed in [22] for a multi-port dc-dc converter. However, as will be discussed below, the switching actions of the primary-side bridge legs are not synchronous any more.

As in [22], all four secondary-side bridge legs operate with a fixed duty cycle of 50% (advantageously resulting in equal stress for the high-side and low-side devices S_{J} and S'_{J}, respectively). **Figure 3** summarizes the modulation, where the secondary-side bridge-leg A is considered as the frame of reference with a per-unit (i.e., normalized to 2π) phase shift $\varphi_{\mathrm{A}} = 0$. To achieve the desired secondary side transformer voltage u_{TA} with an effective duty cycle d_{TA} (e.g., from (1)), the bridge-leg B (forming an H-Bridge together with bridge-leg A across the phase a secondary side transformer winding TA) requires a per-unit phase shift $\varphi_{\mathrm{B}} = \varphi_{\mathrm{A}} + d_{\mathrm{TA}}/2$ of its pulse width modulation (PWM) carrier relative to the master PWM carrier of A. With φ_{B} known, the appropriate per-unit phase shift φ_{C} (relative

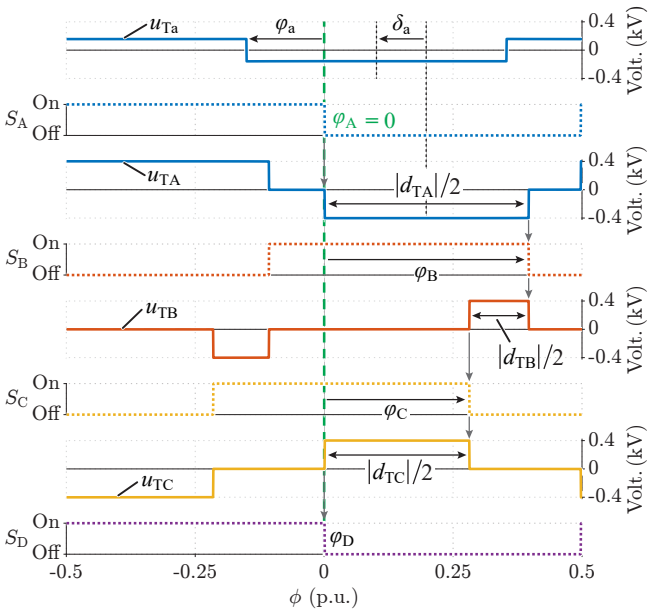

Fig. 3: Modulation of the secondary-side four-leg switching stage according to [22]: Arbitrary effective duty-cycles d_{TJ} of the three secondary-side transformer voltages U_{TJ} can be realized by phase-shifting the switching signals of the four bridge-legs, which all operate with a fixed duty of 50%. Using the PWM carrier of bridge-leg A as the master, i.e., $\varphi_{\mathrm{A}} = 0$, the other per-unit (normalized to 2π) phase shifts φ_{J} are evaluated from top to bottom according to the desired effective duty-cycles d_{TJ}, thus uniquely defining the phase relation of the secondary-side transformer voltages. Further, the top waveform shows the primary-side transformer voltage u_{Ta} to illustrate the calculation of the effective phase angle φ_{a} for the primary-side modulation according to (3).

to PWM carrier A) can be calculated to generate the desired transformer voltage u_{TB}, with the process repeating to finally evaluate the required φ_{D} (here, $\varphi_{\mathrm{D}} = \varphi_{\mathrm{A}}$ results because a symmetrical three-phase system is considered in the example). It is important to highlight that the three secondary-side transformer voltages can have arbitrary duty cycles, but that the phase relation among the three voltages then follows and cannot be freely chosen.

2.2 Control and Standard Modulation

Figure 4 shows the phase-modular control block diagram suitable for three-phase and single-phase operation. The proposed scheme utilizes phase modular control blocks which first use the measured phase voltage u_{j} to provide the ac voltage amplitude $\hat{u}_{\mathrm{j}}$ and phase $\angle_{\mathrm{j}}$ via a phase locked loop (PLL). The phase of the measured ac voltage $\angle_{\mathrm{j}}$ along with the reference and measured grid currents (i_{j}^{*} and i_{j} respectively) are then provided as input to the per-phase (single-phase) current controller according to [23]. Even though being a single-phase (per-phase) current controller, an implementation in the rotating DQ reference frame via calculating a “virtual” orthogonal (i.e., for sinusoidal quantities, 90° delayed) component for each voltage and current [24] is used; the D-axis is oriented at the grid voltage u_{j} and hence $u_{\mathrm{j,D}} = \hat{u}_{\mathrm{j}}$ and $u_{\mathrm{j,Q}} = 0$. The controller then acts on the D- and Q-components of the mains current reference, which, advantageously, are constant and thus facilitate zero steady-state error using PI regulators. Including further the reactive power demand of the ac-side input capacitor as a feedforward term, the algorithm calculates two control parameters: the per-unit, i.e., normalized to 2π, phase shift δ_{j} between secondary and primary-side transformer voltages, and an additional angle $\phi_{\mathrm{m,j}}$ necessary for the reactive power operation discussed in **Section 3.1** (i.e., $\phi_{\mathrm{m,j}} \approx 0$ for nominal ohmic mains operation). A more detailed explanation of the grid current control is beyond the scope of this paper, which focuses on the X-Rectifier modulation, and interested readers are referred to the literature [23], [24]; further, other grid current control methods could be employed.

The values $\hat{u}_{\mathrm{j}}$ and $\angle_{\mathrm{j}} + \phi_{\mathrm{m,j}}$ then are provided as inputs along with the measured EV battery voltage U_{dc} to the duty cycle generation blocks to generate d_{TJ} according to

$$d_{\mathrm{TJ}} = \min\left(\frac{\hat{u}_{\mathrm{j}}}{2U_{\mathrm{dc}}}\frac{N_2}{N_1}, 1\right)\sin\left(\angle_{\mathrm{j}} + \phi_{\mathrm{m,j}}\right), \qquad (2)$$

which are fed to the secondary-side modulator discussed above. For sinusoidal grid voltages, this results in equal voltage time-areas applied to the primary-side and secondary-side windings of the transformers, respectively, and is denoted as the (improved) “standard” modulation M#1. Note that $d_{\mathrm{TJ}} \in [-1, 1]$ accounts for the polarity changes of the ac input voltages u_{j} without the need for any control modifications at zero crossings.

To facilitate power flow control, the aforementioned phase shift δ_{j} between secondary-side and primary-side transformer voltages (which is effectively constant over a mains period with slight variations to correct for minor errors ensuring adequate PFC) must be correctly applied given the defined phase relation among the secondary-side transformer voltages u_{TJ} discussed above, i.e., synchronous switching of the primary-side bridge legs as in [9],

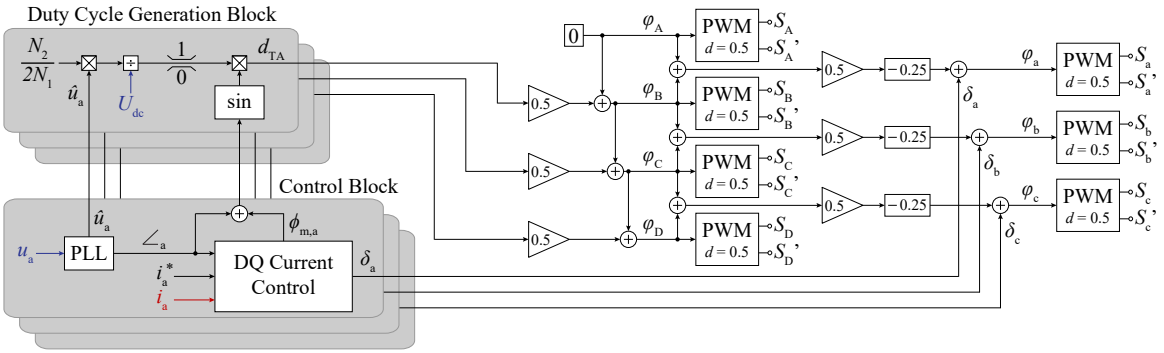

Fig. 4: Proposed phase-modular and three-/single-phase impartial X-Rectifier control scheme, with the (exemplary) per-phase grid current control implemented in a rotating DQ reference frame according to [23]. The phase shift angles δ_j and φ_j are in per unit (i.e., normalized to 2π).

[10], [16], [25] won't be possible. Instead, the per-unit phase shift of the ac front-end half-bridge a,

$$\varphi_\mathrm{a} = \frac{\varphi_\mathrm{A} + \varphi_\mathrm{B}}{2} - 0.25 + \delta_\mathrm{a}, \tag{3}$$

must be applied relative to the master PWM carrier A, as illustrated in **Fig. 3**. Similar calculations for φ_b and φ_c are indicated in **Fig. 4**.
Advantageously, the proposed phase-modular control implementation is impartial to whether the X-Rectifier is connected to a three-phase or single-phase grid (see **Fig. 1a** and **Fig. 1b**, respectively) as the algorithm processes each voltage u_j measured across the input capacitor C_j independently.

2.3 Three-/Single Phase Operation

Figure 2 shows simulated key waveforms of the X-Rectifier operating using the proposed control scheme with the standard secondary-side modulation M#1 and converter specifications/parameters listed in **Tab. 1**, respectively. Note that the dc output capacitance C_dc is designed for filtering of HF switched currents and not as a large storage element for buffering the twice-mains-frequency power pulsation in single-phase operation ([26] found no accelerated ageing of lithium-ion battery cells with 100 Hz charging currents).The resonance frequency f_0 = 17.8 kHz of C_S and L_S is far below the switching frequency f_sw = 72 kHz, which results in transformer currents i_Tj like in a DAB converter. Due to the open-delta winding configuration with the four secondary-side bridge-legs, the bridge-leg currents i_B and i_C are larger in magnitude than i_A and i_D (see **Fig. 2b.ii**).[2]

[2] In a cost-optimized design, the power semiconductors in legs B and C are then selected with a larger chip area (i.e., lower $R_\mathrm{ds,on}$) than those in legs A and D.

In contrast to the proof-of-concept modulation used in [16], the proposed modulation M#1 doesn't suffer from constraints on the transformer turns ratio if single-phase operation should be possible, i.e., a far more favourable transformer turns ratio $N_1 : N_2$ = 1:2 is employed. This in turn drastically reduces the current stress, e.g., the primary-side peak transformer current reduces from $i_\mathrm{Tj} \approx 75$ A in [16] down to 44 A in **Fig. 2** (U_dc = 400 V and P = 6.6 kW); even larger reductions are observed for the secondary side. Furthermore, with the secondary-side modulation M#1, the switching frequency of the secondary side is kept equal to that of the primary-side M-BDS half-bridges, i.e., $f_\mathrm{sw} = 72\,\mathrm{kHz}$, instead of having the secondary side half-bridges operating with up to twice the nominal switching frequency with the proof-of-concept modulation from [16].

3 Extended Functionality

For a major share of the operating time, OBCs simply charge or discharge (V2G) the EV battery from/to a symmetrical three-phase or a single-phase mains as discussed above. However, M#1 also supports the extended functionality of the X-rectifier.

3.1 Reactive Power Support

The grid of the future is expected to be supplied more and more from distributed energy resources (DERs), whereby the batteries of EVs provide valuable energy storage. Therefore, OBCs should be able to provide reactive power support to the grid as required by standards such as, e.g., VDE-AR-N 4105 [27] (minimum reactive power capability of $\cos\phi$ = 0.9 for DERs with a capacity of $>$ 4.6 kVA). Utilizing the proposed control scheme from **Fig. 4** and suitable grid current references

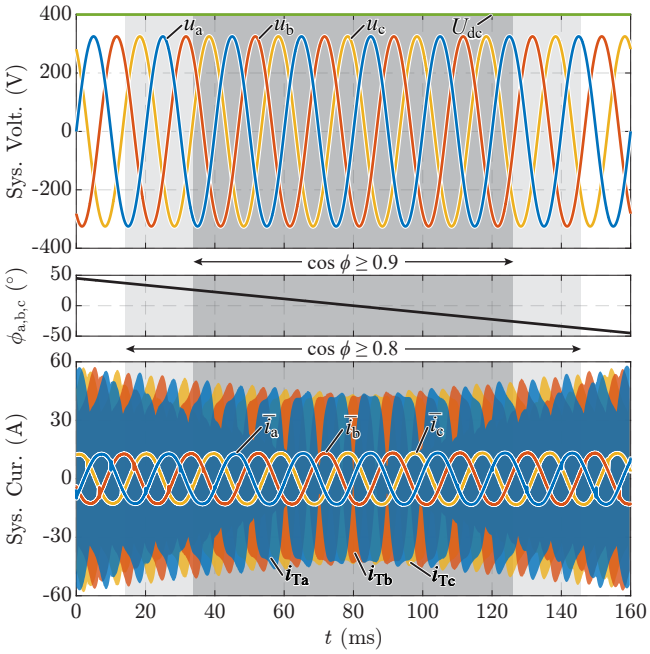

Fig. 5: Simulated reactive power operation of the X-Rectifier at nominal power delivery of 6.6 kW to the battery. A slight increase in current stress is experienced, as expected for decreasing $\cos\phi$.

i_j^*, the X-Rectifier meets and exceeds these requirements with a minor penalty to converter performance as shown in **Fig. 5** (some increase in the current stress is indicated by the transformer currents i_{Ta}, i_{Tb}, i_{Tc}). Note that reactive power support also works in the same way when connected to a single-phase grid.

3.2 Asymmetrical Three-Phase Grid

Further, **Fig. 6** demonstrates charging operation from an asymmetric three-phase mains with the phase a voltage u_a reduced to 50%. The current reference i_a^* (see **Fig. 4**) is reduced proportionally to the phase voltage to implement a grid-friendly ohmic behaviour, i.e., the power reduces to 25% in phase a while the other two phases continue to each deliver their rated 2.2 kW to the output.

3.3 Islanded/Standalone Operation

For example, on a construction site or in case of a power outage, the vehicle battery is a valuable power source and hence the X-Rectifier can form an islanded three-phase grid (i.e., grid-forming or vehicle to load (V2L) operation). Thus, the control scheme from **Fig. 4** is modified such that the ac-side input voltages are closed-loop controlled instead of the ac input current, the duty cycle generation / modulation remains unchanged. In such scenarios, extreme asymmetrical loading of the phases

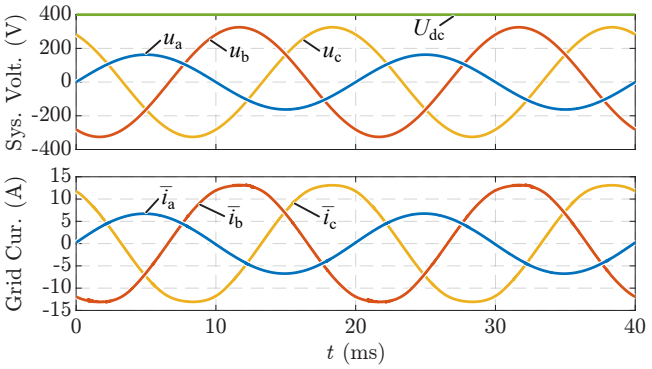

Fig. 6: Simulated charging operation from an asymmetric/unbalanced three-phase grid with ohmic mains behaviour ($i_j^* \propto v_j$ in **Fig. 4**).

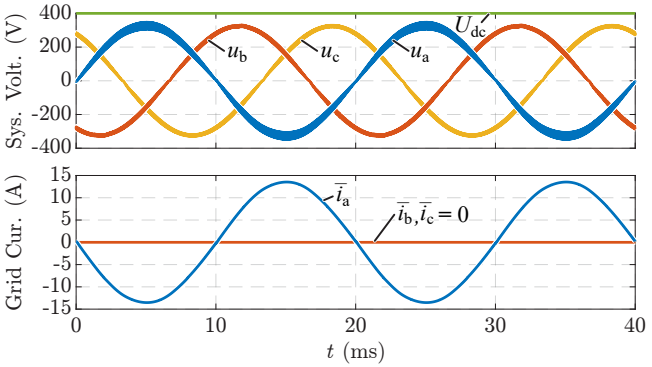

Fig. 7: Simulated islanding/standalone power supply operation of the X-rectifier with only one phase loaded to rated capacity while the other two phases are unloaded.

must be expected as indicated by the waveforms shown in **Fig. 7**, where only phase a delivers nominal 2.2 kW while phases b and c are completely unloaded.

4 Optimized Modulation

To facilitate the optimization of the modulation parameters (and, at a later stage, the converter design) the converter behaviour is modelled in MATLAB. The transformer currents are evaluated in the frequency domain, similar to the work in [28], for a finite number of switching periods distributed evenly over one mains period to reduce computational effort. This numerical approach considers that the dc blocking capacitor C_S and the transformer leakage inductance L_S can be tuned to have a specific resonance frequency f_0 relative to the switching frequency f_{sw}. For this paper, the degrees of freedom in the system design are fixed to those provided in **Tab. 1** (resulting in $f_0 \ll f_{sw}$, i.e., a DAB-type operation with mostly trapezoidal transformer current). However, whereas the choice of the secondary-side

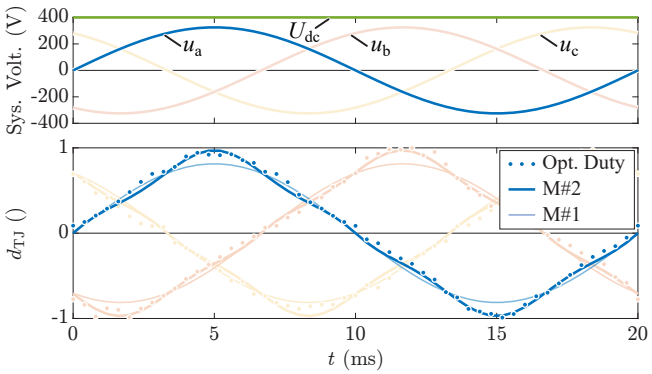

Fig. 8: Optimum (minimum total semiconductor losses) secondary-side duty cycles d_{TJ} over a mains period (P = 6.6 kW and U_{dc} = 400 V), shown as dots, compared against M#1 from (2) and the proposed straightforward approximation (M#2) based on the two-parameter function from (4), which closely tracks the optimal values.

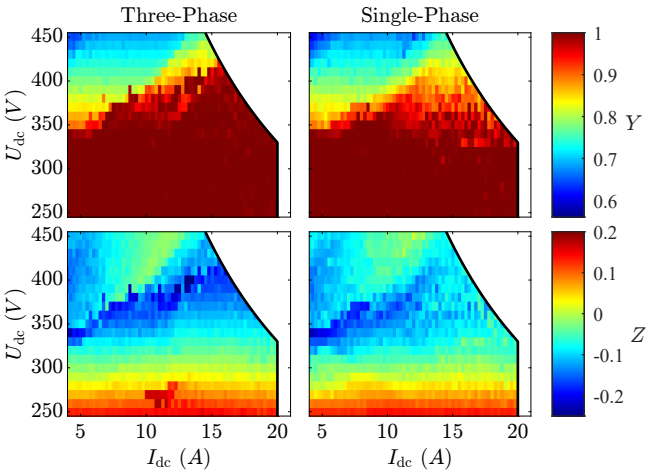

Fig. 9: Optimum modulation parameters Y and Z resulting in minimum total semiconductor losses (conduction and switching) over the operating range of the X-Rectifier for a given grid peak voltage of 325 V.

duty cycles according to (2) such that the voltage-time areas on both sides of the transformer are equal seems a natural choice, it is not necessarily optimum regarding the converter losses, e.g., because of limited zero-voltage switching (ZVS) range, etc.

Clearly, for any combination of ac-side voltages, dc-side voltage, and required power flow, optimum secondary-side duty cycles d_{TJ} could be found as in any DAB converter, e.g., similar to the optimal ZVS modulation method for single-phase ac-dc DAB converters discussed in [29], but with certain constraints as the X-Rectifier's primary-side duty cycles are fixed to 50%. However, such an implementation requires multidimensional look-up tables (LUTs) and the modulation parameters must be extracted essentially for every switching period.

4.1 Optimized Duty Cycles

In a first step, the MATLAB model is run to evaluate the optimal duty cycles d_{TJ} for various switching periods across the mains period, as indicated by the dots in **Fig. 8** for the nominal three-phase operating point of P = 6.6 kW and U_{dc} = 400 V.

The selected optimization goal is to minimize the total semiconductor losses (conduction and switching) considering a loss model of a 25 mΩ Infineon GaN M-BDS and a 25 mΩ unidirectional GaN power transistor (scaled from the loss model in [30]).[3]

However, if all operating points of the X-rectifier should be adequately covered, a large seven-dimensional LUT[4] would be needed.

Instead, we propose approximating the secondary-side duty cycle variation over a grid period (named M#2 in the following) with a straightforward mathematical function that can easily be integrated as the "Duty Generation Block" in the control scheme of **Fig. 4**, i.e.,

$$d_{\mathrm{TJ}} = Y \sin\left(\angle_{\mathrm{j}} + \phi_{\mathrm{m,j}}\right) + Z \sin\left(2(\angle_{\mathrm{j}} + \phi_{\mathrm{m,j}})\right)^2 \operatorname{sgn}\left(\angle_{\mathrm{j}} + \phi_{\mathrm{m,j}}\right), \quad (4)$$

where $j \in \{a, b, c\}$. Note that the resulting trajectories of d_{TJ} in **Fig. 8** match closely the individually optimized values (dots) but deviate from the standard d_{TJ} values (M#1) obtained with (2), especially around the peak grid voltage. Advantageously, this approach requires just two modulation parameters Y and Z, which are optimized for each system-level operating point of the OBC (i.e., combination of three-/single-phase peak voltage, dc output voltage, and output current). **Figure 9** displays the optimum values for Y and Z over the OBC operat-

[3]Junction temperatures are dependent on device thermal models which are coupled via a thermal interface material (TIM), with a thermal impedance of 52 K mm²/W, to a water-cooled cold plate with a (maximum) temperature of 60 °C.

[4]Since the current stress and hence the losses of the secondary-side bridge legs B and C depend on the superposition of *two* transformer currents, it is not possible to reuse the same LUT for the three phases but a combined LUT with a 7-dimensional input (3 separate grid voltages, 3 separate grid powers, and the dc output voltage) is needed.

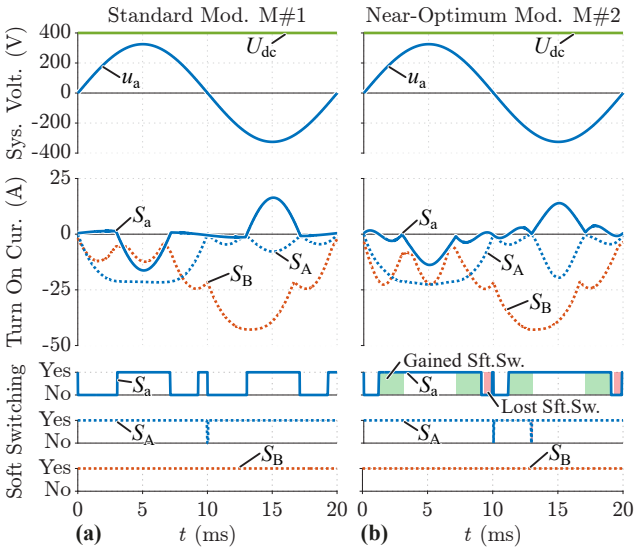

Fig. 10: Simulated turn-on currents of the three switches S_a, S_A and S_B relevant to phase a of the X-Rectifier using the methods **(a)** M#1 with (2) and **(b)** M#2 with (4); M#2 achieves a much wider soft-switching region of the primary-side M-BDS S_a.

ing range given the converter specifications from **Tab. 1**.

The required 3D LUTs (grid peak voltage, output voltage, output current) are thus small and only infrequent look-ups are needed (e.g., once per mains period), which ensures compatibility with commonly available microcontrollers. However, note that operating in one of the extended-functionality modes described in **Section 3** is best done by falling back to M#1 using (2), unless the mentioned implementation using a 7D LUT would be acceptable.

4.2 Soft-Switching Analysis

To provide an overview of the X-Rectifier soft-switching performance utilizing M#1 with (2) and M#2 with (4) and Y = 0.97, Z = -0.15, **Fig. 10** presents simulation results for three-phase operation at nominal power of P = 6.6 kW and a battery voltage of U_{dc} = 400 V. As can be seen from the turn-on currents of the three high-side switches S_a, S_A, and S_B relevant to phase a, M#2 achieves a much wider soft-switching range for the primary-side M-BDS S_a; hard-switching transitions occur only around the grid voltage zero crossing and thus contribute little losses, too. Both methods (M#1 and M#2) ensure almost complete soft-switching of the secondary-side transistors.

4.3 Performance Comparison

The implemented MATLAB model is used to evaluate the system performance in terms of the semi-

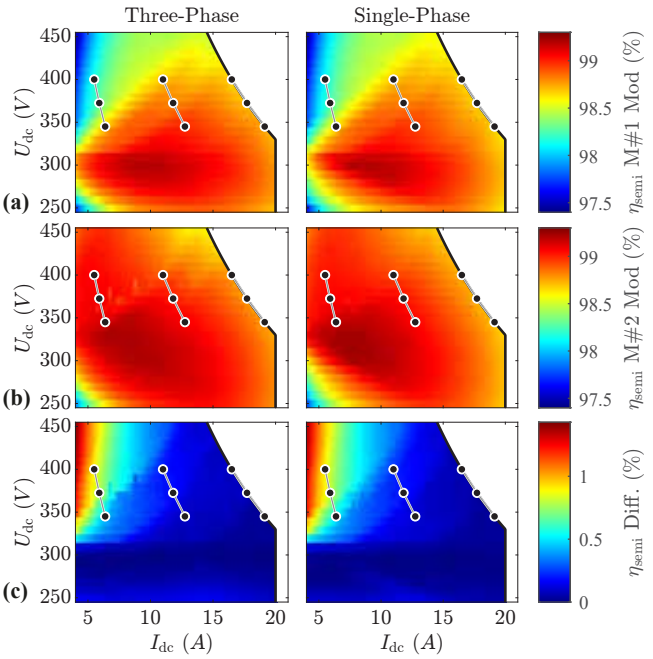

Fig. 11: Calculated semiconductor efficiency η_{semi} of the X-Rectifier using **(a)** M#1 or **(b)** M#2. **(c)** highlights the efficiency improvement achieved with M#2. The dots indicate the operating points considered in the exemplary charging process mission profile (voltage based on battery SOC range and power based on grid connection availability) discussed in the text.

conductor efficiency η_{semi} over the OBC operating range, considering the specifications from **Tab. 1**. First, **Fig. 11a** shows that M#1 achieves nearly identical performance in both, three- and single-phase operation over most of the operating region. The near-optimum approach M#2 shows a further performance improvement, as shown in **Fig. 11b**. The percentage difference between the two methods is shown in **Fig. 11c** and highlights that the improvements are mostly experienced for low power and a high dc output voltage, i.e., a high state of charge (SOC) of the battery.

Figure 11 highlights the wide operating range of the X-Rectifier. However, considering real-world battery-charging applications with a nominal battery pack voltage of 360 V and a typically used state-of-charge (SOC) range of 15%...85%, the voltage of a nickel manganese cobalt (NMC) battery would vary between about 345 V and 400 V, and the voltage of a lithium iron phosphate (LFP) battery only between about 360 V and 380 V according to the open circuit voltages presented in [31]. Therefore, the OBC charging process mission profile relevant for the system optimization is limited to this more narrow voltage range. Fur-

ther, a certain assumption on the availability shares of three-phase and single-phase grid connection points with specific power ratings must be made. Whereas these could be based on market studies, we consider here equal shares of single-phase and three-phase charging at three power levels ($\frac{1}{3}P$, $\frac{2}{3}P$ and P considered). An exemplary mission profile could thus consist of three SOCs of a NMC battery of 15%, 50% and 85% with time-shares of 25%, 50% and 25%, and three common power levels of $\frac{1}{3}P$, $\frac{2}{3}P$ and P with equal time shares, and equal time spent in three-phase and single-phase mode (resulting in the points indicated in **Fig. 11**). This results in a weighted semiconductor efficiency of $\bar{\eta}_{\mathrm{semi}}$ = 98.6% for M#1 and $\bar{\eta}_{\mathrm{semi}}$ = 98.9% for M#2, i.e., a reduction of the semiconductor losses by about 20%.

In absolute terms, note that the presented semiconductor efficiencies are for the system specifications from **Tab. 1**, i.e., further improvements could be achieved by using an outer optimization loop to identify more suitable converter parameters (e.g., L_{S}, f_0, $N_1 : N_2$ ...), which is subject of future work.

5 Conclusion

This paper proposes an improved standard modulation method for the single-stage isolated eXtended-functionality rectifier (X-Rectifier) for next-generation EV OBCs, which significantly reduces the transformer and transistor current stresses and expands the soft-switching range compared to a previously published proof-of-concept modulation method. Using the proposed modulation methods (M#1 and M#2), the control concept enables decoupled bidirectional power flow regulation in the three ac grid phases and hence is impartial regarding operation with a three- or single-phase grid in terms of control and performance (i.e., no power derating and effectively equal efficiency). Further, the proposed standard method M#1 is applicable to all extended functionality scenarios (asymmetrical three-phase grid, reactive power injection, islanding/standalone mode with heavily imbalanced phase loading). Further refinements of M#1 have been investigated via a numerical optimization routine and a straightforward implementation of the secondary-side duty cycle without the need for high-dimensional LUTs and suitable for implementation on standard microcontrollers while still achieving near-optimal semiconductor losses has been introduced (approach M#2). Compared to M#1, the charging process mission profile semiconductor efficiency improves from $\bar{\eta}_{\mathrm{semi}}$ = 98.6% to 98.9% for M#2, corresponding to a 21% decrease in semiconductor losses. Further research will utilize the numerical optimization framework to optimize the X-Rectifier converter parameters for a high-power-density demonstrator.

Acknowledgment

The Advanced Mechatronic Systems Group at ETH Zurich is generously supported by the *Else und Friedrich Hugel Fonds* via the ETH Zurich Foundation, for which the authors are most grateful. The authors would also like to thank Dr. Matthias Kasper and Dr. Gerald Deboy from Infineon Technologies AG for samples of the GaN M-BDS devices and their insights on the requirements of next-generation OBCs.

References

[1] H. Wouters and W. Martinez, “Bidirectional onboard chargers for electric vehicles: State-of-the-art and future trends,” *IEEE Trans. Power Electron.*, vol. 39, no. 1, pp. 693–716, Jan. 2024.

[2] K. Ali, R. K. Surapaneni, *et al.*, “An SiC-MOSFET-based nine-switch single-stage three-phase AC–DC isolated converter,” *IEEE Trans. Ind. Electron.*, vol. 64, no. 11, pp. 9083–9093, Nov. 2017.

[3] J. Lee, H. Jeong, *et al.*, “Three-phase single-stage bidirectional CCM soft-switching AC–DC converter with minimum switch count,” *IEEE Trans. Power Electron.*, vol. 38, no. 2, pp. 2052–2062, Feb. 2023.

[4] J. W. Kolar, U. Drofenik, and F. Zach, “Vienna Rectifier II—A novel single-stage high-frequency isolated three-phase PWM rectifier system,” *IEEE Trans. Ind. Electron.*, vol. 46, no. 4, pp. 674–691, Aug. 1999.

[5] N. D. Weise, K. K. Mohapatra, and N. Mohan, “Universal utility interface for plug-in hybrid electric vehicles with vehicle-to-grid functionality,” in *Proc. IEEE PES Gen. Meeting*, Minneapolis, MN, Jul. 2010.

[6] J. J. Sandoval, S. Essakiappan, and P. Enjeti, “A bidirectional series resonant matrix converter topology for electric vehicle DC fast charging,” in *Proc. IEEE Appl. Power Electron. Conf. Expo. (APEC)*, Charlotte, NC, USA, Mar. 2015, pp. 3109–3116.

[7] M. J. Harrison, “A cyclo-converter and methods of operation,” WO2008018802A2, Feb. 2008.

[8] Y. Kosesoy, R. Bonten, *et al.*, "Control of a zero-voltage switching isolated series-resonant power circuit for direct 3-phase AC to DC conversion," in *Proc. Europ. Conf. Power Electron. Appl. (EPE/ECCE Europe)*, Hanover, Germany, Sep. 2022.

[9] D. Menzi, F. Krismer, *et al.*, "Novel bidirectional single-stage isolated three-phase buck-boost PFC rectifier system," in *Proc. IEEE Appl. Power Electron. Conf. Expo. (APEC)*, Orlando, FL, USA, Mar. 2023.

[10] R. Baranwal, K. V. Iyer, *et al.*, "A reduced switch count single-stage three-phase bidirectional rectifier with high-frequency isolation," *IEEE Trans. Power Electron.*, vol. 33, no. 11, pp. 9520–9541, 2018.

[11] E. Asa, O. C. Onar, *et al.*, "A novel three-phase Oak Ridge AC/DC converter for wireless EV charger applications," in *Proc. IEEE Appl. Power Electron. Conf. Expo. (APEC)*, Phoenix, AZ, USA, Jun. 2021, pp. 437–443.

[12] M. Zhang, H. Zou, *et al.*, "A novel single-stage bidirectional isolated three-phase resonant mode AC-DC PFC converter," in *Proc. Energy Convers. Congr. Expo. (ECCE USA)*, Nashville, TN, USA, Oct. 2023, pp. 2222–2229.

[13] J. E. Bosso, M. Llomplat, *et al.*, "Isolated bidirectional DC-to-three-phase AC converter for integration of renewable energy sources to electric grid," *IET Power Electron.*, vol. 12, no. 8, pp. 2058–2068, 2019.

[14] B. P. Do, M. Gerado Geda, *et al.*, "Single-phase and three-phase compatible single-stage OBC with 6-switches secondary side," in *Proc. Energy Convers. Congr. Expo. (ECCE Asia)*, Chengdu, China, May 2024, pp. 1908–1912.

[15] H. Kim, J. Park, *et al.*, "A single-stage electrolytic capacitor-less EV charger with single- and three-phase compatibility," *IEEE Trans. Power Electron.*, vol. 37, no. 6, pp. 6780–6791, Jun. 2022.

[16] D. Zhang, S. Weihe, *et al.*, "Single-stage isolated bidirectional extended-functionality X-Rectifier for EV chargers with three/single-phase AC input capability," in *Proc. Energy Convers. Congr. Expo. (ECCE USA)*, Phoenix, AZ, USA, Oct. 2024.

[17] Infineon Technologies AG, *Infineon announces CoolGaN bidirectional switch*, https://www.infineon.com/cms/en/about-infineon/press/market-news/2024/INFPSS202406-111.html, Jun. 2024.

[18] D. Bisi, "GaN bidirectional switches: The revolution is here," *IEEE Power Electron. Mag.*, vol. 12, no. 1, pp. 29–36, Mar. 2025.

[19] N. Schibli, "Symmetrical multilevel converters with two quadrant DC-DC feeding," Ph.D. dissertation, EPFL, Lausanne, Switzerland, 2000.

[20] D. Boillat, S. Roy, *et al.*, "Design considerations of a three phase dual active bridge based on reactive power flow," in *Proc. IEEE Energy Convers. Congr. Expo. (ECCE USA)*, Raleigh, NC, USA, Sep. 2012, pp. 424–430.

[21] N. D. Weise, G. Castelino, *et al.*, "A single-stage dual-active-bridge-based soft switched AC–DC converter with open-loop power factor correction and other advanced features," *IEEE Trans. Power Electron.*, vol. 29, no. 8, pp. 4007–4016, Aug. 2014.

[22] T. Ohno, S. Mirić, *et al.*, "New triple-output quad-active-bridge DC/DC converter employing a four-leg inverter input stage," in *Proc. Int. Conf. Electr. Machines. Syst. (ICEMS)*, Zhuhai, China, Nov. 2023, pp. 3984–3991.

[23] N. Weise and L. Doiron, "DQ current control of a bidirectional, isolated single-stage AC-DC converter," in *Proc. IEEE Appl. Power Electron. Conf. Expo. (APEC)*, Fort Worth, TX, USA, Mar. 2014, pp. 1888–1893.

[24] R. Zhang, M. Cardinal, *et al.*, "A grid simulator with control of single-phase power converters in D-Q rotating frame," in *Proc. IEEE Power Electron. Specialists Conf. (PESC)*, Cairns, Australia, Jun. 2002, pp. 1431–1436.

[25] M. Zhang, H. Zou, *et al.*, "Double Y-configuration multi active bridge converter: A single stage bidirectional AC-DC converter with simple sinusoidal control," Oct. 2024, URL: https://arxiv.org/abs/2410.21440.

[26] A. Bessman, R. Soares, *et al.*, "Aging effects of AC harmonics on lithium-ion cells," *J. Energy Stor.*, vol. 21, pp. 741–749, Feb. 2019.

[27] VDE Verband der Elektrotechnik Elektronik Informationstechnik e.V., *VDE-AR-N 4105*.

[28] M. Zhang, J. Tong, *et al.*, "A unified numerical modeling method for dual active bridge type converter," in *Proc. Energy Convers. Congr. Expo. (ECCE USA)*, Phoenix, AZ, USA, Oct. 2023, pp. 3035–3041.

[29] J. Everts, F. Krismer, *et al.*, "Optimal ZVS modulation of single-phase single-stage bidirectional DAB AC–DC converters," *IEEE Trans. Power Electron.*, vol. 29, no. 8, pp. 3954–3970, Aug. 2014.

[30] D. Menzi, Z. Yu, *et al.*, "Comparative evaluation of ultra-lightweight buck-boost DC-DC converter topologies for future eVTOL aircraft," in *Proc. Control Modeling Power Electron. Workshop (COMPEL)*, Tel Aviv, Israel, Jun. 2022, pp. 1–8.

[31] M.-K. Tran, A. DaCosta, *et al.*, "Comparative study of equivalent circuit models performance in four common lithium-ion batteries: LFP, NMC, LMO, NCA," *Batteries*, vol. 7, no. 3, p. 51, Sep. 2021.